A Probabilistic Framework for Correlation Assessment and Combination of Multisite Paleoseismic Data: Evidence for Accelerated Strain Release Along the Altyn Tagh Fault

Nicolás Pinzón*[1,2] and Yann Klinger[1]

ABSTRACT

The timing of past earthquakes is generally represented in the form of probability density functions (PDFs). The integration of this data from multiple sites is essential to investigate the size, spatial–temporal organization, and recurrence of large earthquakes along active fault systems. In this work, we introduce a new framework for integrating event-age PDFs from multiple sites into a unified earthquake chronology. Since a large rupture is defined by the overlap of PDFs from different trench sites, we implement the Bhattacharyya coefficient to compare earthquake PDFs and quantify the overlap degree for contemporaneous events. This approach enables a quantitative assessment of all possible rupture correlations. Second, we develop a weighted-mean method to combine overlapping PDFs into a single distribution representing the time of the rupture. These methodologies are implemented in multisite integrated chronologies (MUSIC), an open-source toolbox for correlation assessment and combination of paleoseismic data. MUSIC offers the potential to improve earthquake probability assessments along major fault systems. We demonstrate the use of MUSIC tools to better constrain the timing of large, clustered earthquakes along the central–eastern sections of the Altyn Tagh fault (ATF). The weighted-mean method yields narrower age uncertainties than the conventional mean approach while preserving contributions from all correlated paleoseismic datasets. Then, we compute earthquake recurrence intervals along the ATF using a Monte Carlo approach that accounts for event-age uncertainties. We found that the recurrence behavior shows a regular increase in the frequency of large earthquakes during clustering periods. Therefore, if the central–eastern ATF is currently in a cluster phase, the ~370-yr elapsed time implies elevated probabilities of an M 7.0+ earthquake occurring within the next decades.

1

KEY POINTS

- How can we integrate multiple paleoseismic datasets to achieve a comprehensive rupture history of a fault?
- We introduce the multisite integrated chronologies (MUSIC) toolbox for objective correlation and combination of paleoseismic datasets.
- MUSIC reduces uncertainty in earthquake chronologies for more reliable seismic hazard assessments.

Supplemental Material

INTRODUCTION

Paleoearthquake time series capture the temporal organization of large earthquakes along active fault systems over multiple seismic cycles. They are essential for constraining models of earthquake recurrence, whether based on time-independent Poisson processes (Gerstenberger *et al.*, 2020) or time-dependent forecasting approaches (Wang *et al.*, 2024). In this context, paleoseismology plays a central role in reconstructing the past seismic behavior of faults to determine the present and future seismic hazard to society. Certainly, reconstructing a precise paleoseismic history of any fault is inherently challenged by

1. Université Paris Cité, Institut de Physique du Globe de Paris (IPGP), CNRS, Paris, France, https://orcid.org/0000-0003-4467-929X (NP); https://orcid.org/0000-0003-2119-6391 (YK); 2. Physical Science and Engineering, King Abdullah University of Science and Technology, Thuwal, Saudi Arabia

*Corresponding author: npinzonmatapi@gmail.com

Cite this article as Pinzón, N., and Y. Klinger (2026). A Probabilistic Framework for Correlation Assessment and Combination of Multisite Paleoseismic Data: Evidence for Accelerated Strain Release Along the Altyn Tagh Fault, *Bull. Seismol. Soc. Am.* **XX**, 1–17, doi: 10.1785/0120260103

uncertainties related to the geological resolution of the trench sites. This resolution depends on multiple factors, such as intermittent or continuous sedimentation, varying degrees of preservation, geological hiatuses due to erosional processes or prolonged periods of nondeposition, the availability of datable material, and the inherent uncertainties associated with the dating methods employed (e.g., terrestrial cosmogenic nuclides, luminescence, or radiocarbon). Since these factors may differentially affect specific areas, the quality and completeness of the sedimentary record can vary considerably between different paleoseismic sites along the same fault system. Therefore, integrating paleoseismic data from multiple sites becomes essential to generate a more robust and complete paleoearthquake chronology, either at local or regional scales.

In paleoseismology, the ages of past earthquakes documented in trenches are expressed as probability density functions (PDFs), each representing an uncertainty model that encapsulates the possible timing of the event. The integration of such data from multiple paleoseismic sites generally involves two main operations: correlation and combination. The correlation between event ages consists of comparing PDFs from different trench sites to establish temporal overlaps between paleoearthquake ages. This step is also critical for determining the potential spatial extent of past earthquakes and for distinguishing events that may have ruptured one or multiple fault sections. Once the correlation between sites is proposed, a probabilistic procedure is required to date the rupture from the different event ages contributed by each site. The combination step addresses this by collapsing the correlated PDFs into a single probability distribution. This resulting distribution provides a consensus estimate of the age of the large rupture by considering the full range of available paleoseismic evidence. Some methods have previously been proposed to estimate correlations between event age PDFs (e.g., Biasi and Weldon, 2009) and to combine probability distributions (e.g., Biasi and Weldon, 2009; DuRoss *et al.*, 2011; Gómez-Novell
2 *et al.*, 2023). Although these approaches have provided useful frameworks for correlating and combining event-age PDFs, they could benefit from methods that more explicitly recognize the epistemic uncertainties inherent in paleoseismic observations, thereby providing event-age estimates that better reflect the full range of available evidence.

In this work, we present multisite integrated chronologies (MUSIC), a framework based on probabilistic methods that aims to integrate multisite paleoseismic data into a single paleoearthquake chronology. We apply the MUSIC tools along the Altyn Tagh fault (ATF), a major active left-lateral strike-slip fault located in the northern edge of the Tibetan plateau (Fig. 1). A surface trace of about 1100-km-long attests of the occurrence of large earthquakes along the ATF (Chinese State Bureau of Seismology, 1992). However, since the beginning of instrumental records, only four fault-rupturing earthquakes have been documented: In 1924, two large earthquakes of magnitudes M_w 7.0 and 7.2 ruptured the westernmost section of the fault (Gu, 1983). More recently, in the southwestern ATF junction area, two earthquakes, M_w 7.1 and 6.9, occurred in 2008 and 2014, respectively (Xu *et al.*, 2011; Li *et al.*, 2015; Li *et al.*, 2020). By contrast, no large instrumental earthquake 3
($M_w > 7.0$) has been recorded along the central–eastern sections of the ATF. Fortunately, paleoseismic investigations have provided crucial insights into the long-term rupture behavior of this fault system (Pinzon *et al.*, 2024). The central–eastern 4
section consists of two active strands: the northern (NATF) and the southern (SATF) strands, which are separated by a 15-km-long compressional bend (Fig. 1). Yuan *et al.* (2018) extended the earthquake chronology in the Xorxoli section located in the SATF. Shao *et al.* (2018) documented past ruptures in the compressional bend, where the NATF and SATF spatially overlap. Then, Luo *et al.* (2019) investigated the paleoseismic history of the Tashi section, located at the easternmost end of the NATF. These paleoseismic investigations characterized the rupture behavior at the scale of individual fault sections. On the other hand, Pinzon *et al.* (2024) investigated the rupture history of the fault at both local and regional scales. They applied the integration approach of Biasi and Weldon (2009) to combine paleoseismic data from three new trenches in the Aksai section of the NATF and paleoearthquake evidence from the aforementioned fault sections. Through this synthesis, Pinzon *et al.* (2024) proposed a regional rupture model in which large earthquakes along the southern and northern strands synchronized and released strain in temporal clusters, punctuated by millennial periods of seismic quiescence of the fault system.

Using the Pinzon *et al.* (2024) rupture model as a reference, we introduce and test MUSIC an open-access toolbox for integrating paleoseismic data across multiple spatial scales (codes are available in Data and Resources). MUSIC consists of two main steps designed to first assess correlations and then to combine paleoseismic datasets. First, we propose the Bhattacharyya coefficient (BC) as a statistical tool to evaluate the overlap degree between contemporaneous PDFs (Fig. 2a). Second, the weighted-mean method is developed to combine event-age PDFs from multiple sites into a refined regional chronology of large earthquakes (Fig. 2b). Finally, we investigate rupture patterns of the fault system, by applying a Monte Carlo-based approach to estimate recurrence intervals along the ATF and their uncertainties (Fig. 2b). Altogether, MUSIC not only advances our understanding of rupture behavior along the ATF, but is also broadly applicable to other fault systems, representing a step toward more reliable seismic hazard assessments in tectonically active regions that represent a risk to the present-day society.

PALEOSEISMIC DATASET

In this study, we used available paleoseismic data from previously published investigations conducted along the ATF between 2001 and 2024 (Fig. 1, Table S1, available in the supplemental material

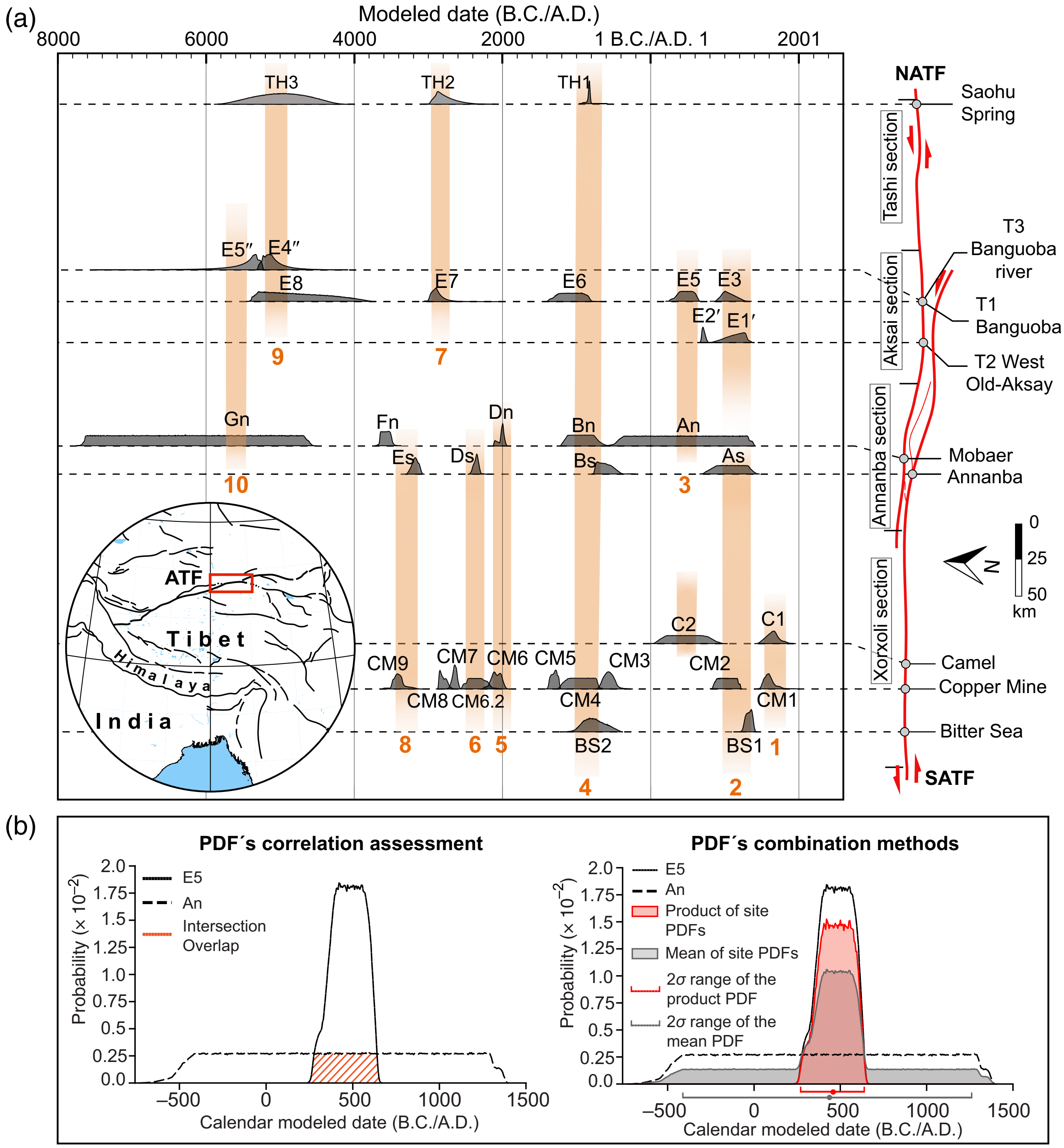

119 **Figure 1.** (a) Event age probability density functions (PDFs) from nine different trench sites used to test the multisite integrated chronologies (MUSIC) methodology (modified from Pinzon *et al.*, 2024). The inset in the lower-left corner shows the structural map of the Tibetan plateau. The open red square marks the central–eastern Altyn Tagh fault (ATF), which is enlarged in the right panel of panel (a). The trench locations are shown as solid gray circles along the fault trace of the central–eastern ATF. PDFs are labeled according to the original author nomenclatures (see table 5.1). The vertical orange stripes correspond to temporal rupture correlations proposed by Pinzon *et al.* (2024). Event 1 is supported by dated offset markers, PDF overlap, and trench-based observations (ranked event indicators). Events 2 and 3 are supported by PDF overlap, dated offset markers, historical records, and trench-based observations (ranked event indicators). Events 4 and 7 are constrained by PDF overlap and cumulative offset markers. Events 5, 6, 8–10 are supported by PDF overlap and trench-based observations, including chronostratigraphic constraints and ranked event indicators. The event recurrence and rupture lengths of these events are also consistent with empirical slip–rupture length relationships (Wells and Coppersmith, 1994) and the long-term slip rate of the fault. (b) Events E5 and An are used to represent current methodologies to integrate paleoseismic data. On the left side, orange stripes represent the intersection overlap commonly used to measure the overlap degree of two PDFs. On the right side, the gray curve represents the resulting PDF from the mean of the two overlapping PDFs (Biasi and Weldon, 2009). The red curve results from the normalized product of the two overlapping PDFs (DuRoss *et al.*, 2011). The color version of this figure is available only in the electronic edition.

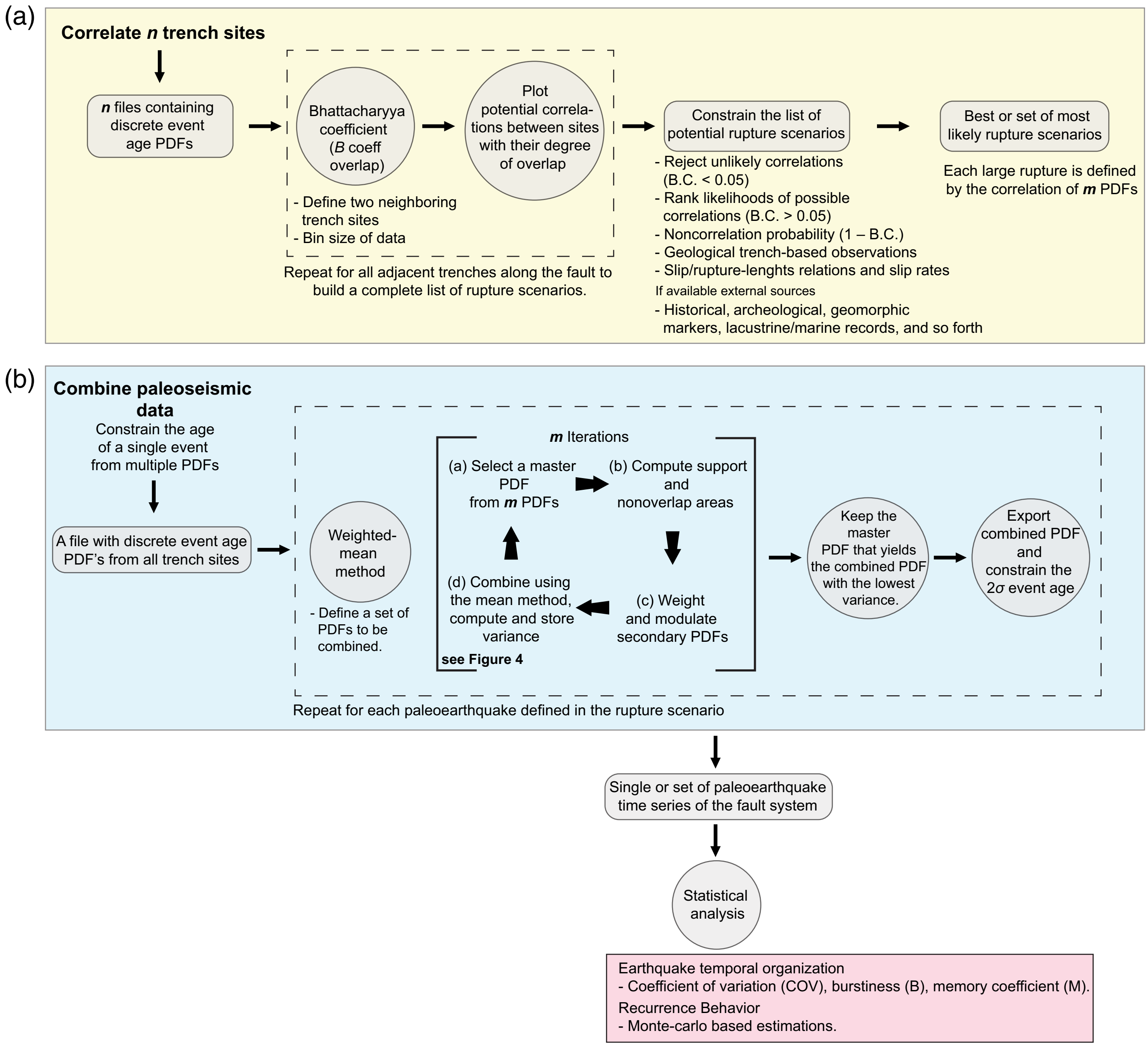

Figure 2. MUSIC workflow for paleoseismic data integration: (a) the correlation assessment between neighboring trench sites (yellow box), and (b) the combination of multiple PDFs into a single or set of chronologies (blue box). The rectangles correspond to input files or discrete products, with the text below indicating relevant elements. The circles denote statistical/ 20
probabilistic processes, with the text below specifying parameters to be predefined. Methodologies within the red box correspond to postprocessing statistical analysis, also accessible through MUSIC. The color version of this figure is available only in the electronic edition.

to this article). Thirty-five PDFs constraining surface rupture evidence from nine trench sites along the central–eastern ATF were used to implement MUSIC. We only considered events supported by high-quality ground rupture indicators, according to Scharer *et al.* (2007). These event-age PDFs define a set of correlations corresponding to ten large paleoearthquakes that ruptured one or multiple fault sections across the Tashi, Aksai, Annanba, and Xorxoli sections over the last 8 ka (Pinzon *et al.*, 2024). Although the event-age PDFs are primarily supported by high-quality ground rupture indicators, the rupture correlations proposed by Pinzon *et al.* (2024) were also informed by trench stratigraphy, low-ranked events indicators, and the absence of contemporaneous deformation at some sites, geomorphic, and historical observations, which were used to evaluate alternative rupture scenarios. Therefore, in this work we do not aim to discuss the different possibilities of event correlations along the ATF; we rather use the rupture correlations defined by Pinzon *et al.* (2024) as a reference to introduce and test an objective statistical metric for quantifying the degree of overlap between event-ages and combine multiple PDFs.

Event ages reported with 95% confidence intervals, mean ages, trench locations, and corresponding references are listed in Table S1 and represented in Figure 1a. Each PDF in Figure 1 represents the probability that an earthquake occurred at a given time. These PDFs can be generated using Bayesian model frameworks (e.g., OxCal 4.4; Bronk-Ramsey, 2008). In practice, OxCal first generates age models from raw radiocarbon (^{14}C) measurements, which are calibrated into calendar ages. The age model can be refined by incorporating additional chronological constraints such as historical records or stratigraphic relationships. Stratigraphic information is particularly useful when radiocarbon samples can be ordered relative to each other in the sediment deposits; in such cases, OxCal allows users to define "sequences" when a clear order of events exists, or "phases" when samples can only be grouped without strict ordering (Lienkaemper and Bronk Ramsey, 2009). These options enable the construction of event-age models that accurately reflect the geological context of the trench data and provide robust probability density functions for paleoearthquake occurrence.

MUSIC FRAMEWORK FOR PALEOSEISMIC DATA INTEGRATION

In the following sections, we introduce the MUSIC framework, which consists of two methodological stages that aim first at the correlation assessment and then at the combination of paleoseismic data. We also compare these methodologies with previously proposed approaches, highlighting both their contributions and limitations, particularly when dealing with event-age uncertainties.

Quantifying PDF overlap across multiple sites

The first step in integrating paleoseismic data is to identify possible correlations between event-age probability distributions (PDFs) from different sites, to recognize potential earthquakes that may have ruptured one or multiple fault segments. This process involves comparing PDFs from two neighboring trench sites to evaluate whether there is any temporal overlap (Figs. 1b and 2a). Then, when such an overlap is identified, a single rupture involving both sites could be defined. The rupture extent of a given paleoearthquake can be further expanded when there is systematic overlap among consecutive pairs of site PDFs, or when a "master" site (i.e., one with a longer and well-resolved record) shows overlap with a third site, which in turn overlaps with a fourth, and so on. This cascading overlap can help define rupture correlations at regional scales (Fig. 1a).

To quantify the degree of overlap between PDFs from different sites, Biasi and Weldon (2009), proposed to compute the intersection area as shown in equation (1) (Fig. 1b), which consists of the sum of the minimum probabilities between two
5 PDFs, A and B:
6

$$\mathrm{Intersection(A,B)} = \sum \min(P_{\mathrm{A}}(t_i), P_{\mathrm{B}}(t_i)). \qquad (1)$$

Here, t_i represents time bins of the discrete date PDFs, and P is the probability that an earthquake occurred within each bin for events A and B. The minimum function reasonably captures the amount of overlap between two uniform or Gaussian probability distributions. However, this approach might underestimate the overlap when comparing two asymmetric PDFs, even if they are well aligned in time. This is because the overlap reflects only the minimum probability at each time bin. For example, a narrowly constrained distribution overlapping a broader one yields a low overlap area, not due to the poor temporal agreement, but rather because it measures the smallest area between the two PDFs (see event E5 and An in Fig. 1b). This limitation makes the minimum function an inconsistent metric for assessing the overlap, particularly when dealing with asymmetric and unequally constrained PDFs often obtained from OxCal models. To address this limitation, we propose to use the Bhattacharyya coefficient (BC) as a more robust and informative measure of overlap, as shown in equation (2):

$$\mathrm{BC(A,B)} = \sum \sqrt{(P_{\mathrm{A}}(t_i) \times P_{\mathrm{B}}(t_i))}. \qquad (2)$$

The BC simultaneously captures both the temporal alignment and the shape similarity between two probability density functions (Bhattacharyya, 1943). Its values range from 0 to 1, where BC = 1 corresponds to two distributions with identical shapes that are fully overlapped in time, and BC = 0 indicates no overlap. Unlike the minimum probability method, which only accounts for the smallest shared probability at each time bin, the BC smoothly weights the joint probability. As a result, in cases where one distribution is narrowly peaked and the other is broader, the computed overlap reflects contributions from both probability distributions (Fig. 3a), rather than being dominated by the lower probability values. When the BC between two probability distributions is < 0.05, the distributions are considered as significantly different (Guillerme and Cooper, 2016). Therefore, we suggest that, for the purpose of evaluating potential rupture correlations, BC values below this threshold, such as those observed between Fn–E8, Dn–E7, and An–E6 (Fig. 3b), should not be considered sufficiently robust to establish a correlation.

Given the central role of this metric in assessing correlations, it is also important to consider how the BC compares with other statistical approaches commonly used to evaluate chronological consistency and event synchronicity. The OxCal agreement index and chi-square statistics are potential alternatives (Bronk, 2001; Bronk Ramsey, 1995). However, the agreement index is intended to estimate whether a posterior distribution is consistent with a reference age measurement, instead of quantifying the overlap between two posterior PDFs from different Bayesian models. Similarly, a chi-square approach is primarily designed as a hypothesis test evaluating whether two PDFs are statistically compatible rather than measuring an overlap magnitude. Furthermore, asymmetric and long-tailed PDFs may disproportionately influence the chi-square statistic, as small expected probabilities in the tails can amplify minor differences between

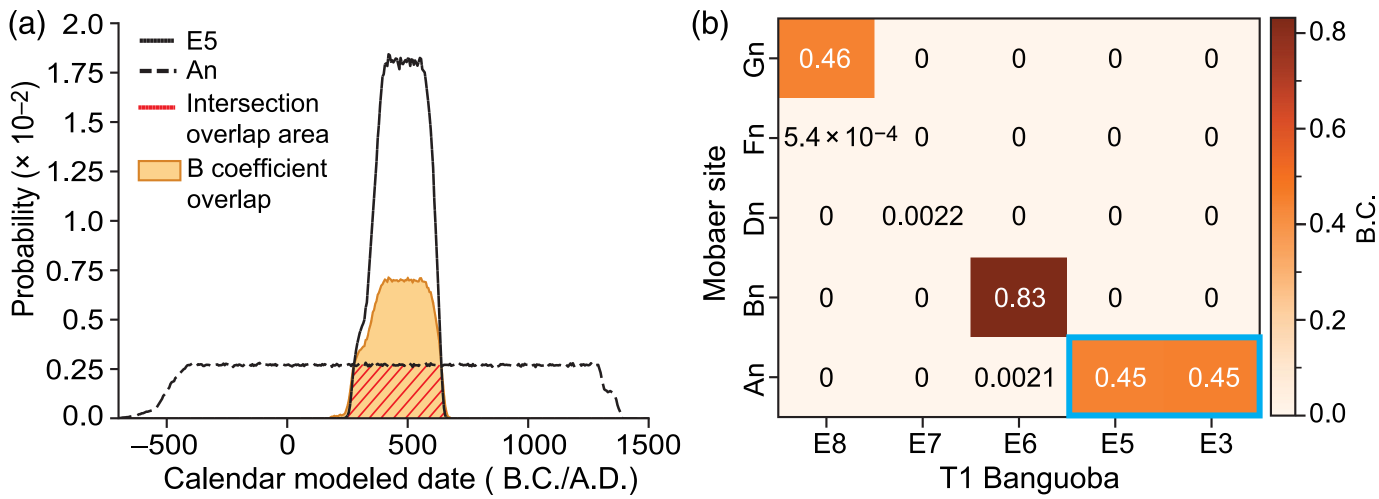

Figure 3. PDF overlap estimation and correlations. (a) The Bhattacharyya coefficient (BC) method to compare two PDFs (E5 and An events). The red lines defined the intersection area. The brown curve represents the overlap area using the BC approach. (b) Correlation matrix between events from the T1 Banguoba site and Mobaer site. The color scale represents the degree of similarity between PDFs quantified by the BC. The blue rectangle highlights an overlap of two events (E5 and E3) from the T1 trench with one event (An) at Mobaer. The color version of this figure is available only in the electronic edition.

distributions. Thus, we favor the BC, which directly provides a direct, symmetric, and consistent measure of probabilistic overlap.

Bridging data and multisourced observations: An integrative approach to earthquake correlation

In the process of assessing different possible PDF correlations, a common outcome when comparing PDFs from multiple locations is the emergence of multiple possible overlaps, and thus, more than one plausible correlation (Cinti *et al.*, 2021). This typically occurs when a wide PDF at one site overlaps with two or more narrow PDFs at a neighboring site, potentially leading to several plausible rupture scenarios. Gómez-Novell *et al.* (2023) argued that, given the large uncertainties sometimes associated with event ages, all overlapping PDFs between adjacent sites should be treated with equal weight in the preferred rupture scenario. Although this observation could be valid in a purely data-driven process, rupture correlations between paleoseismic sites are difficult to demonstrate on the basis of probability distributions alone (Biasi *et al.*, 2002). One consequence of this limitation is the potential over- or underestimation of the number and size of past earthquakes. For example, in Figure 3b, we compare event age PDFs from trench T1 with events at Mobaer site (see also Fig. 1). Event An from T1 shows a temporal overlap with two different events, E5 and E3, documented at Mobaer (Fig. 3a). Based solely on a PDF analysis, we might have considered three possible scenarios: (1) a single large rupture (~150 km long), represented by either An-E5 or An-E3; (2) two large ruptures involving both An-E5 and An-E3; or (3) three different smaller paleoearthquakes. At this stage, the BC can be regarded as an objective tool for a probabilistic assessment of such correlation scenarios. However, favoring a particular scenario based only on the BC metric may be misleading. Figure 3b illustrates this limitation, showing identical BC values for the An-E5 and An-E3 correlations. For this reason, we highlight that MUSIC does not automatically produce or favor one rupture scenario based solely on BC values.

Considering chronologically constrained offsets and the lack of evidence of recent fault scarps on the northern strand of the Annanba section, event An is interpreted to be distinct from and older than E3 (Elliott *et al.*, 2015; Shao *et al.*, 2018). In addition, trench-based observations show that deformation indicators of E5 are stronger than E3 and comparable with the rank index of secondary deformation observed for An. These observations led Pinzon *et al.* (2024) to support a single correlation between An and E5, corresponding to a large rupture approximately 150 km long, consistent with historical records and average fault displacements of 5.3 m along the Aksai section.

In this section, we do not revisit all possible correlations among paleoseismic records along the ATF, as these have already been comprehensively evaluated by Pinzon *et al.* (2024) and each proposed correlation is summarized in the caption to Figure 1. Besides, in the MUSIC framework, we emphasize that integrating multiple independent lines of evidence is essential for discriminating among competing correlations. Key sources for validating rupture models include: (1) earthquake catalogs, historical records, and archaeological data (Wechsler *et al.*, 2014; 7
Benjelloun *et al.*, 2018; Pinzón *et al.*, 2021); (2) geological observations at individual trench sites, such as the presence of unconformities, potential chrono- and lithostratigraphic correlations, and the quality and frequency of vertical deformation indicators (Klinger *et al.*, 2015; Pinzon *et al.*, 2024); (3) geomorphological evidence, particularly chronologically constrained offset markers, which have been used to support rupture correlations and estimate earthquake magnitudes (Elliott *et al.*, 2015); (4) lacustrine/marine paleoseismology, used as high-resolution 8
sedimentary archives to expand the record of prehistoric earthquakes (Kremer *et al.*, 2017); and (5) consistency between

rupture lengths with cumulative slip displacements and slip rates (Biasi and Weldon, 2009).

Combining PDFs from multiple sites into a single earthquake chronology

Large earthquakes identified through temporal correlations are represented by multiple overlapping event-age PDFs, which can be combined into a unified paleoearthquake chronology to better constrain their timing. For example, event 4 is defined based on the overlap between CM4, Bn, E6, BS2, Bs, E6, and TH1 (Fig. 1a). At this stage, we combine the probabilities of all these PDFs to produce a single distribution that synthesizes the available chronological information for event 4. Then, the same approach is applied to other potential ruptures defined along the fault system.

Two main procedures have been proposed to combine contributing PDFs. Biasi and Weldon (2009) introduced the mean method, which involves directly summing the probabilities and dividing by the total number of contributors (Fig. 1b). Later, DuRoss *et al.* (2011) proposed the product method, which involves computing the direct product of probabilities for each corresponding time bin between overlapping probability distributions. Although the latter is widely used because it significantly narrows the resulting event age uncertainty (Fig. 1b), it requires careful consideration.

The product method assumes that the most likely timing of a paleoearthquake lies within the overlap region of contemporaneous PDFs. Although this assumption is reasonable, the method exclusively favors the full overlap region and consequently the best-constrained (i.e., narrowest) distribution. The direct product produces progressively narrower age estimates as additional PDFs are incorporated, whereas disregarding the shapes of the equally contributing PDFs and penalizing regions of partial overlap by reducing their probabilities to zero. As noted by DuRoss *et al.* (2011), this approach is best suited for integrating paleoseismic data with strong degrees of confidence in the correlation of PDFs across sites. However, such confidence is rarely warranted, particularly at regional scales, where correlations among site PDFs are more uncertain due to poor overlaps. In such cases, the product method may lead to an abrupt overconstrained estimate of the event age, while neglecting the epistemic uncertainties inherent in the full ensemble of paleoseismic observations.

Consequently, the direct product method may not be an appropriate operation to combine event-age PDFs from multiple sites. Nonetheless, one of its foundation assumptions is worthy of consideration; namely, that the likelihood of the event age is higher in the region of full overlap among PDFs than in areas of only partial overlap (DuRoss *et al.*, 2011). We therefore seek an alternative method that preserves this principle while treating each contributing PDF as a valid estimate of the paleoearthquake age. The mean method (Biasi and Weldon, 2009) follows this logic by averaging equally weighted contributing PDFs. The trade-off, however, is that the combined PDF may remain broad when some of the contributing PDFs are poorly constrained.

Weighted-mean method

As an alternative method to combine multiple correlated PDFs, we propose to use a weighted-mean method, which is a straightforward and objective approach to constrain the age of past earthquakes. This method builds on a consensus between the key assumptions of the product method and the probabilistic foundations of the mean method. In doing so, it aims to probabilistically favor the overlap between the full ensemble of contributors, without neglecting the uncertainties from nonoverlap regions between PDFs. The weighted-mean method (Figs. 2b and 4) is described as follows:

1. Define the master PDF: the optimal master PDF emerges as a consensus probability distribution. Namely, it represents the distribution that best captures the common temporal information shared by all paleoseismic datasets. It serves as the reference distribution against which all correlated PDFs are evaluated (Fig 4a). Its probabilities are preserved during the weighting procedure, whereas the secondary PDFs are modulated according to their overlap with the master PDF. The resulting weighted distributions are subsequently combined into a single earthquake chronology. To avoid subjective selection based on perceived data quality, age-model performance, or individual PDF sharpness, each correlated PDF is evaluated as a candidate master distribution, and the final solution is selected from the ensemble of possible combinations. The candidate that yields the most constrained combined distribution, represented by the smallest uncertainty range, is selected as the master PDF (Fig. 2b).
2. Computing weights based on the support and nonoverlap areas: secondary PDFs (TH3 and E8) are divided into two regions relative to the master PDF (E4″; Fig. 4b). The support area corresponds to the region of the secondary PDFs that overlap in time with the master PDF (areas A and M in 9
Fig. 4b). The nonoverlap area corresponds to the region of the secondary PDF that falls outside the time span of the master PDF (areas B and N in Fig. 4b).

For instance, to compute the support and nonoverlap areas A and B, we define a subset *S* that contains the time bins where the product between the probabilities of both distributions, E4″ and TH3, is greater than zero (equation 3). The summation of the TH3 probability density over the subset *S* returns the support overlap area A (equation 4). In parallel, we define a second subset, *S*, containing the time bins where the product of the probabilities from both distributions is zero (equation 5). The sum of the probability densities of TH3 over the subset *S* yields the nonoverlap area B (equation 6). Then, the same procedure is applied to calculate the support overlap area M and the nonoverlap

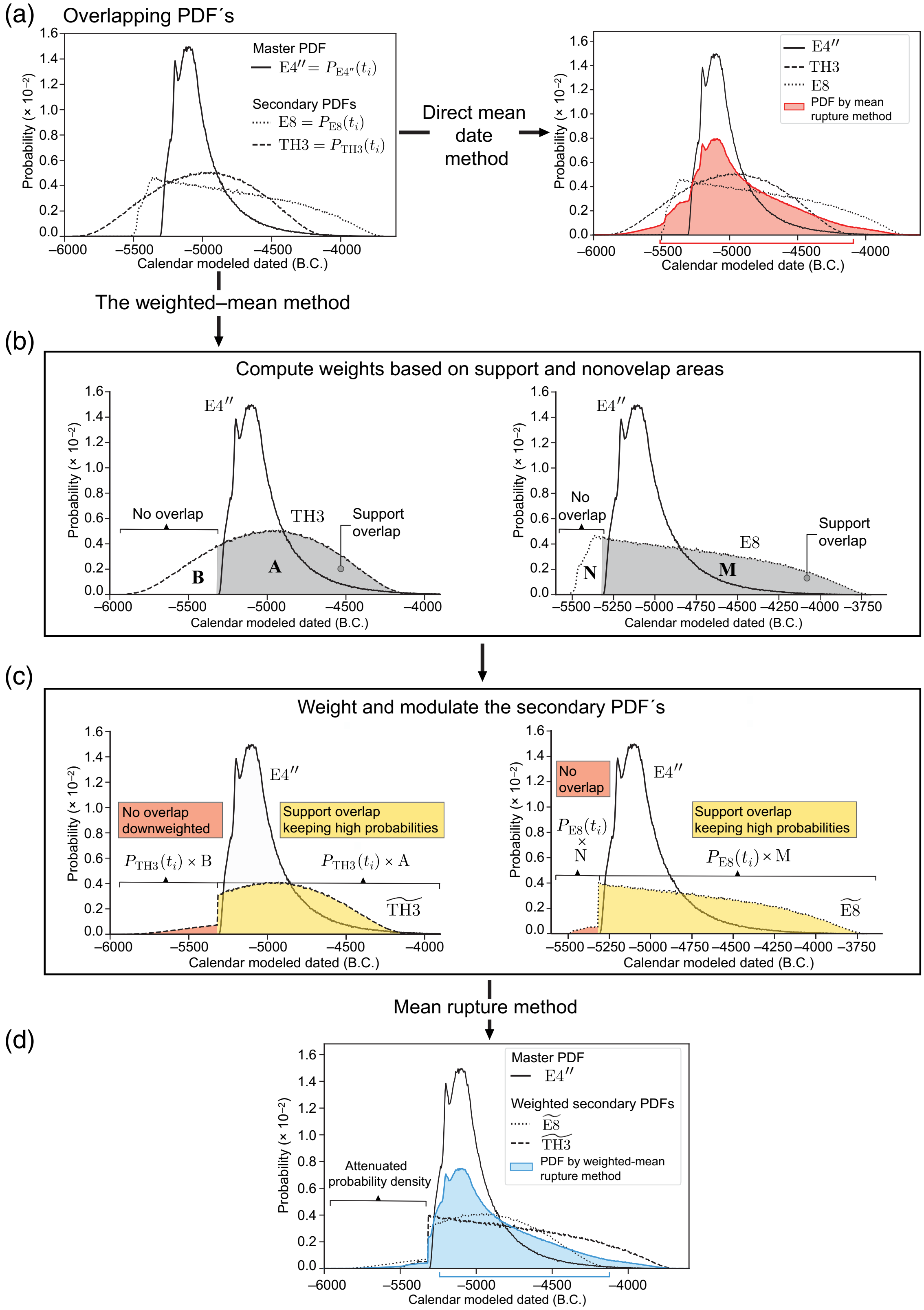

Figure 4. Weighted-mean method to combine paleoseismic data. As an example, rupture correlations among events E4″, TH3, and E8 are used to illustrate the comparison between the direct mean method and the weighted-mean method. The rectangles indicate the mathematical operations carried out at each stage of the workflow. The gray shading marks the support overlap areas of secondary PDFs relative to the master PDF. The red curve shows the combined PDF obtained with the mean method, with its 95% confidence interval indicated by horizontal red lines. The light-blue curve shows the PDF derived from the weighted-mean method, along with its corresponding 95% confidence interval (horizontal blue lines). The color version of this figure is available only in the electronic edition.

area N of E8 (secondary PDF) relative to the master E4″:

$$S = \{t_i | P_{E4''}(t_i) \times P_{TH3}(t_i) > 0\}, \quad (3)$$

$$A = \sum_{t_i \in S} P_{TH3}(t_i) dt, \quad (4)$$

$$\bar{S} = \{t_i | P_{E4''}(t_i) \times P_{TH3}(t_i) = 0\}, \quad (5)$$

$$B = \sum_{t_i \in \bar{S}} P_{TH3}(t_i) dt. \quad (6)$$

3. Weight and modulate the secondary PDFs: This step focuses on modulating the secondary PDFs by down-weighting the nonoverlap areas while preserving high probabilities on the support areas. In the example shown in Figure 4c, the TH3 distribution is modulated to produce a new PDF, $\widetilde{TH3}$, by applying the weights derived from the previous step (Fig. 4c). Specifically, each of the probabilities associated with the time bins in subset S are multiplied by the support overlap area A, whereas the probabilities corresponding to the bins in subset $\bar{S}$ are multiplied by the nonoverlap area B (equation 7). In this case, the support area (A) is larger than the nonoverlap area (B). However, when a narrower PDF correlates with a much broader one, the situation is reversed, and the support overlap becomes smaller than the nonoverlap (Fig. 3a). In such cases, the weighting factors are adjusted accordingly: probabilities within the overlap region would be scaled by 1−A, whereas those in the nonoverlap region would be scaled by 1−B. The same logic applies to other secondary PDFs. Overall, in this stage, we aim to reshape the initially broad and equally weighted secondary PDFs into locally adjusted distributions, where their contribution is scaled according to how consistently they align with the master PDF:

$$\widetilde{TH3} = P_{\widetilde{TH3}}(t_i) = \begin{cases} P_{\widetilde{TH3}}(t_i) \times A, & \text{if } t_i \in S \\ P_{\widetilde{TH3}}(t_i) \times B, & \text{if } t_i \in \bar{S} \end{cases}. \quad (7)$$

4. Combined master and weighted PDFs: Finally, the reweighted secondary PDFs ($\widetilde{TH3}$,$\widetilde{E8}$)are combined with the master PDF (E4″) to generate a single earthquake chronology (blue PDF in Fig. 4d). This final step is achieved using the average method, which ensures that the resulting PDF incorporates contributions from all sites. We highlight that the support and nonoverlap regions are defined relative to the selected master PDF, and that the resulting chronology is therefore influenced by this choice. To minimize potential bias associated with any single distribution, every candidate PDF is iteratively evaluated as a master distribution (Fig. 2b). The final solution is then selected from the ensemble of possible combinations rather than being prescribed a priori. As shown in Figure 4d, the resulting PDF reduces the 2σ uncertainty range by 13% relative to the PDF produced by the direct application of the mean method.

APPLICATION ON REAL PALEOSEISMIC DATA: THE CENTRAL–EASTERN ATF

Assessing rupture correlations from multiple sites

We test the MUSIC framework using the rupture correlations proposed by Pinzon *et al.* (2024) along the central–eastern ATF as a reference model. This model identifies ten large paleoearthquakes that ruptured either single or multiple fault sections (Fig. 1). First, to assess the confidence of the proposed correlations, we computed the BC between trench-site PDFs and compared the results with overlap estimates obtained using the conventional intersection-area approach. We selected the T1 Banguoba and Copper Mine trenches as master reference sites due to their extended paleoearthquake records along the southern and northern strands of the ATF, respectively. The Banguoba trench was compared with four nearby sites, Saohu Spring, T3 Banguoba River, T2 West Old-Aksay, and Mobaer, along the NATF. Similarly, the Copper Mine site was compared with the Bitter, Camel, and Annanba trenches along the SATF. Finally, we included a comparison between the Mobaer and Annanba sites to evaluate potential cross-bridge correlations, as these two sites are located closest to one another across the restraining stepover of the ATF.

In Figure 5, we present the overlap values between paired PDFs associated to each of the ten large earthquakes interpreted by Pinzon *et al.* (2024). When considering the average intersection area, the results reveal a broad range of overlap degrees, with values as low as 0.15 for event 8 and as high as 0.7 for event 1 (Fig. 5a). Notably, events 2–4, and 8 include one or more pairwise correlations characterized by relatively low overlap values (∼0.2), such as CM2–BS1, E5–An, Bs–CM4, and CM9–Es. Although these low values may suggest unlikely correlations, they arise because the method underestimates the true degree of similarity between PDFs that are unequally constrained. This underestimation arises from particular cases identified in our data, which are in fact usual in most datasets: (1) a very broadly constrained PDF that fully overlaps with a narrowly constrained PDF, as in E6–TH1 (supporting event 4) and E5–An (supporting event 3); (2) a highly peaked, sharply defined PDF overlapping only with the tail of another PDF, such as CM2–BS1 (supporting event 2) and CM4–Bs (supporting event 4); and (3) overlapping PDFs with disparate peak probabilities, as seen in CM9–Es (supporting event 8). In all these cases, the overlap area is limited by the smaller height of the two PDFs, which may misleadingly suggest a poorly supported correlation despite significant chronological coherence between the events (Fig. 5a).

Conversely, since the BC accounts for both temporal alignment and shape similarity, it provides a more reliable and consistent metric to assess the quality of overlap. For the same three cases described earlier, the BC assigns a higher level of

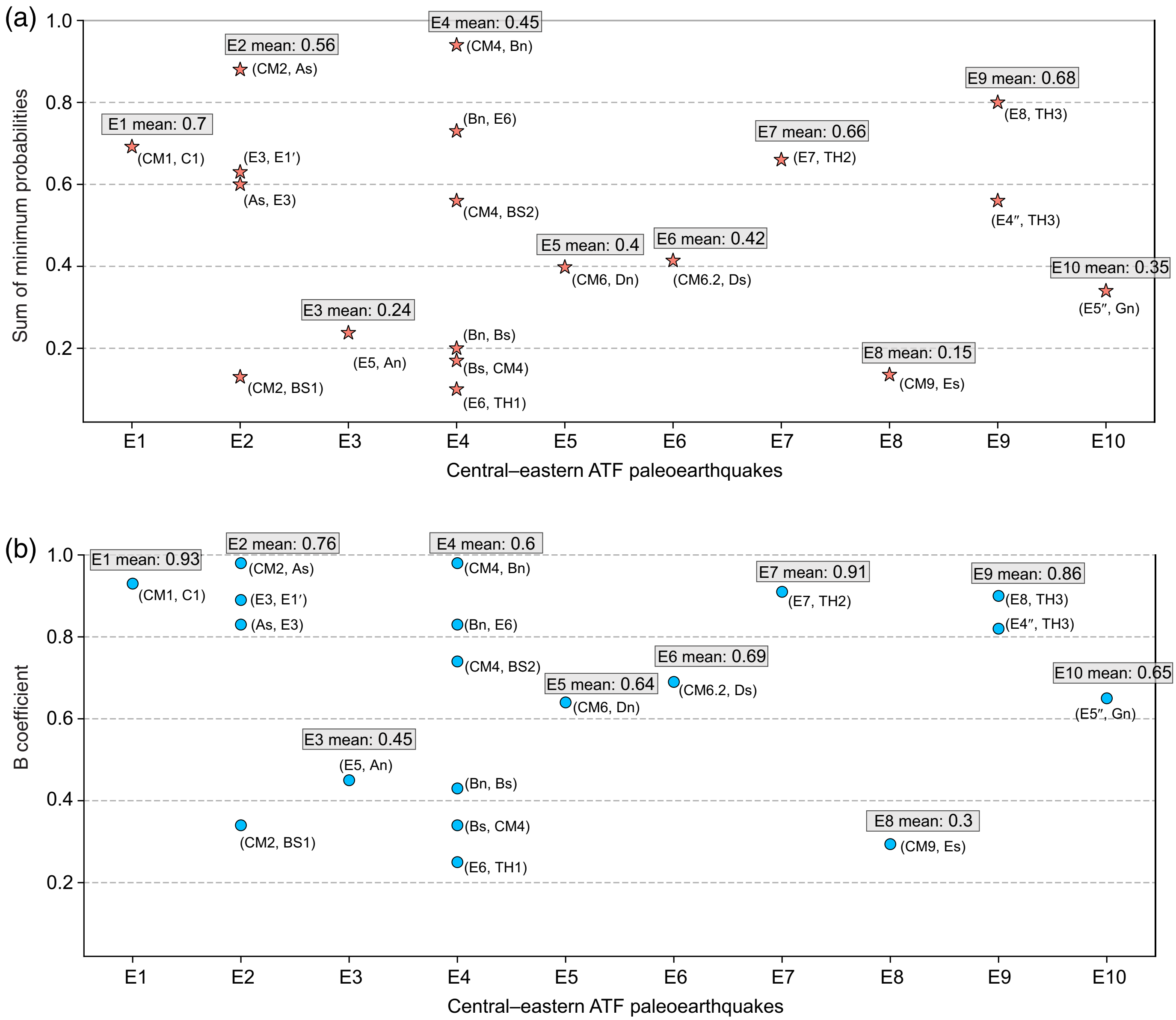

Figure 5. Overlap values for all the contributing and correlated PDFs that defined ten large earthquakes along the central–eastern ATF. (a) The red stars represent overlap values obtained from the intersection area proposed by Biasi and Weldon (2009). (b) The blue circles correspond to overlap values obtained from the BC approach proposed in this work. Values in gray rectangles correspond to the average score for each rupture. The color version of this figure is available only in the electronic edition.

confidence to the overlap between the corresponding PDFs (Fig. 5b). For instance, event 8 was originally regarded as an unlikely correlation by Pinzon *et al.* (2024), based on an overlap intersection area of only 15% between the CM9 and Es site PDFs (Fig. 5a). Such a low overlap would be discarded as a valid temporal correlation according to the thresholds used by Biasi and Weldon (2009). In contrast, the BC yields a 30% of probabilistic agreement between the CM9 and Es events, which in turn corresponds to a temporal overlap of 190 yr. Based on this degree of contemporaneity, together with the strong event indicators identified at both the Copper Mine and Annanba trench sites, the correlation was considered the most plausible interpretation (Yuan *et al.*, 2018; Pinzon *et al.*, 2024). Nevertheless, the degree of nonoverlap (1 − BC = 0.70) remains substantial and warrants consideration. Therefore, the possibility that CM9 and Es represent distinct, smaller earthquakes might not be completely excluded. A similar situation is observed for event 3, whereas the intersection area suggests low confidence degrees, the BC reveals a 45% agreement, representing a temporal overlap of 390 yr between E5 and An. Events 5, 6, and 10 yield intersection area values of 0.4, 0.42, and 0.35 (Fig. 5b), respectively, suggesting moderate levels of temporal correlation. On the other hand, the BC yields values of 0.64 (event 5), 0.69 (event 6), and 0.65 (event 10), indicating a high probabilistic agreement and temporal alignment. Finally, this approach highlights the strong PDF overlaps for events 1, 7, and 9, as well as several contributing overlaps to events 2 and 4. For such events, the BC yields values greater than 0.8 (Fig. 5b), thus quantitatively supporting these rupture correlations with the highest index in terms of PDF similarity. These results underscore the limitations of conventional overlap metrics and highlight the BC as a reliable and useful quantitative tool for assessing the consistency and plausibility of regional earthquake-rupture correlations based on paleoseismic data.

Refining earthquake chronologies along the ATF

The weighted-mean method yields event age PDFs with substantially narrower timing uncertainties, compared with the mean date method used to construct the paleoearthquake chronology in Pinzon *et al.* (2024) (Figs. 6 and 7a). Based on the 95.5% (2σ range) confidence intervals as reference, our method significantly reduces uncertainty ranges, from several decades to hundreds of years. For instance, the 2σ uncertainty ranges for events 5 and 6 are reduced by 80 and 30 yr, respectively (approximately 24% and 13%), when using the weighted-mean method. Furthermore, substantial reductions are observed for events 3, 9, and 10, where the uncertainty ranges decrease by 280, 185, and 425 yr, respectively, which is equivalent to 17%, 13%, and 16% reductions compared with the mean date method (Fig. 6c,i,j). This refinement in the 2σ range reflects a more efficient redistribution of probability, with lower weights assigned to regions of partial overlap contributed by broadly constrained PDFs.

Most paleoruptures (e.g., events 2, 5, 6, 9, and 10) derived from the weighted-mean method exhibit a proportional reduction in uncertainty relative to the ranges obtained from PDFs combined using the direct mean, with the 2σ and 1σ intervals decreasing by similar relative amounts (Fig. 6b,e,f,i,j). Such proportional reductions suggest that the master and secondary PDFs are comparable in shape and timing, producing smooth and normal-skewed distributions consistent with their high B-coefficient values (Fig. 5b). In contrast, some events, such as event 3, represent an exception. The 1σ uncertainty range is reduced nearly three times more than the 2σ range relative to the mean date method (Fig. 6c). This difference arises because the contributing PDFs (An and E5) differ markedly in shape, with one being narrowly constrained and the other considerably broader. Their combination concentrates most of the probability mass within the narrow overlap region, whereas the broader tails retain substantially lower weights.

If the product method were applied to combine An and E5 (event 3), the result would be an even more pronounced reduction in uncertainty, with the 2σ age range shrinking by 70.3% compared with the 2σ range obtained with the mean method (Fig. 1b). By contrast, our weighted-mean method provides a more conservative result, reducing the 2σ range by about 17% (Fig. 6c). As an additional point of comparison, the weighted-mean method assigns a 68.3% probability that event 3 occurred between A.D. 335 and A.D. 595 (Fig. 6c), whereas the product method suggests a probability of 86.1% for the same interval (Fig. 1b). This highlights how the direct product can overconstrain an event age, artificially increasing certainty by zeroing out regions of nonoverlap that still hold plausible dating information.

Events 4 and 8 (Fig. 6d,h) show similar behavior to event 3, being characterized by only moderate PDF overlaps. Thus, using the product method to resolve their ages would abruptly narrow the uncertainty ranges, masking the variability inherent in the paleoseismic data. By contrast, events 1 and 7 exhibit strong PDF similarity, with BC values greater than 0.9 (Fig. 5b); in these cases, the 2σ uncertainty ranges remain largely unchanged regardless of the combination method applied (Fig. 6a,g).

EARTHQUAKE RECURRENCE ALONG THE CENTRAL–EASTERN ATF

Pinzon *et al.* (2024) identified ten paleoearthquakes over the last ~8 ka on the central–eastern sections of the ATF. A quantitative characterization of the paleoearthquake time series, using the memory coefficient (see Goh and Barabási, 2008), revealed a temporal cluster organization, with four earthquakes occurring in the mid-Holocene (events 5–8 in Fig. 7a) and three events in the late Holocene (events 1–3 in Fig. 7a), punctuated by millennial quiescence periods. They argued that these clusters were formed by large earthquakes (M_w 7.5–7.8) rupturing multiple segments of either the NATF or SATF synchronously, as a result of long-term fault interactions. In addition, they identified a potential major event ($M_w > 8$, event 4 in Fig. 7a) that may have breached the barrier between the NATF and SATF and ruptured both strands simultaneously.

In the following section, we aim to evaluate how our refined earthquake chronology constrains mean recurrence-time estimates relative to the original paleoearthquake series of Pinzon *et al.* (2024), while preserving the uncertainty represented by the ensemble of paleoseismic observations.

Computing earthquake recurrence from paleoearthquake time series

To compute the recurrence intervals between successive earthquakes, we applied a Monte Carlo (MC) approach to sample individual event age probability density functions (Fig. 2b). For ten paleoearthquakes temporally constrained along the central–eastern ATF (Fig. 7a), we considered all the 5-year time bins within the 2σ range of each combined PDF. From each distribution, we randomly drew a subset of 100 samples and calculated the pairwise differences between successive events, yielding 100 recurrence intervals for each event pair. The average of these values provides a first-order estimate of the mean interevent time between two events. Then, to ensure that these estimates are not influenced by random sampling variability and to assess the stability of the estimated mean recurrence intervals, we repeated the simulation 1000 times. To preserve the chronological order of the paleoearthquake sequence,

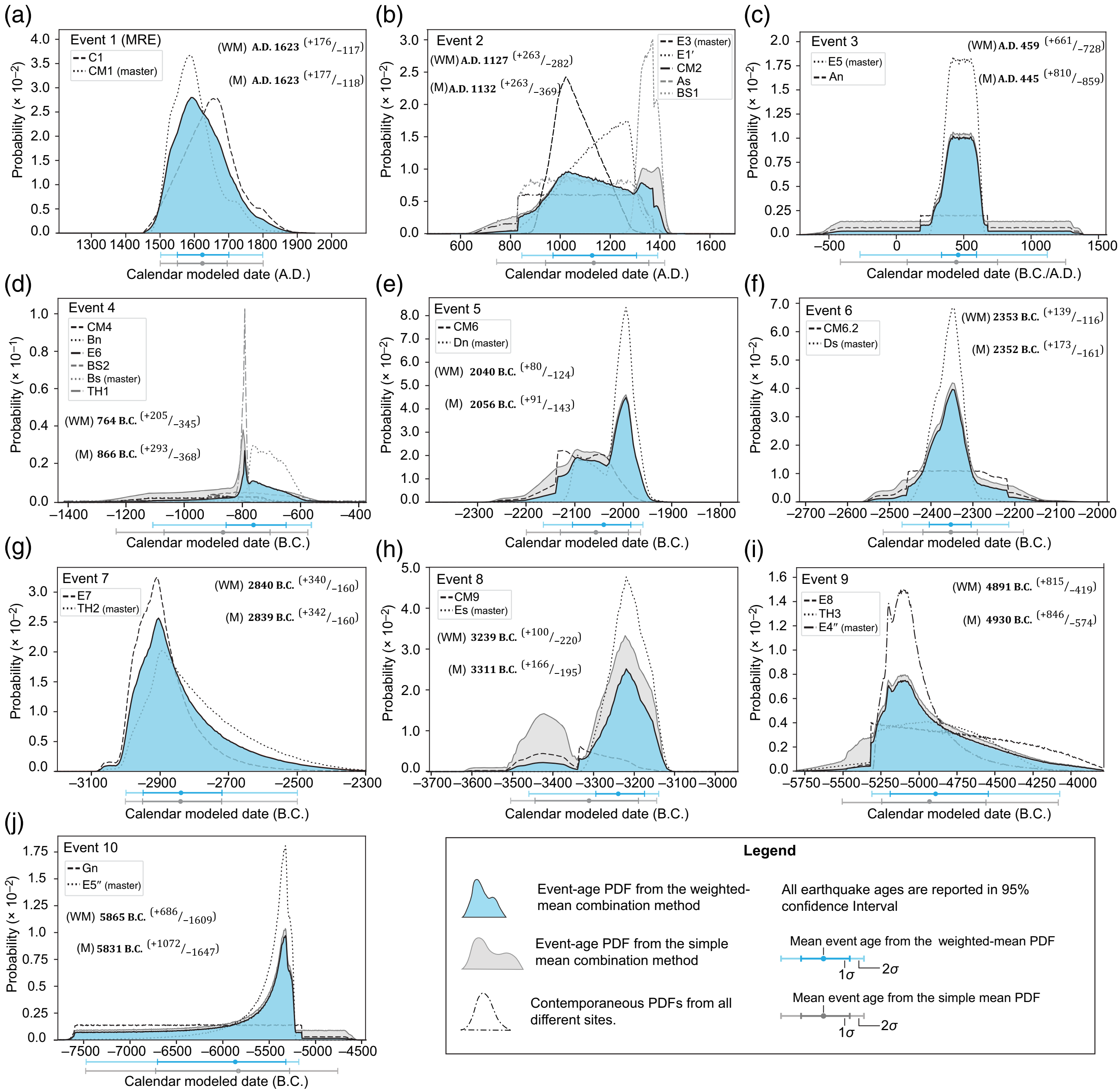

Figure 6. Combined PDFs representing the event age of ten paleoruptures defined from the predefined correlations in Figure 1a. (a–j) Events 1–10, respectively. The light-blue-shaded PDFs were obtained using the weighted-mean method. The gray-shaded areas were derived from the mean date method. The horizontal bars below each plot represent the 2σ and 1σ uncertainty ranges of the event ages. The dotted, dashed, and solid black line curves represent individual contributing PDFs from the different trench sites. The color version of this figure is available only in the electronic edition.

samples yielding temporally inconsistent event ages were discarded and resampled before calculating the mean recurrence intervals. This approach allows for a robust frequency distribution of mean recurrence intervals between successive earthquakes (Figs. S1 and S2). Then, from these distributions, we derive confidence intervals, which are ranges that are likely to contain the unknown recurrence times between events (Fig. 7b). The MC approach is incorporated into the MUSIC framework, where it is available for the analysis of paleoseismic data.

Weighted-mean PDFs yields more precise estimates of mean interevent times than mean-date PDFs (Fig. 7b; Figs. S1 and S2). This is evident by computing the standard error propagation, as shown in equation (8):

$$\sigma_x = \sqrt{\sigma_1^2 + \sigma_2^2 + \ldots + \sigma_n^2}. \tag{8}$$

In this formulation, σ_x represents the total propagated uncertainty resulting from the independent contributions of uncertainties associated with each interevent time ($\sigma_1 \ldots \sigma_n$).

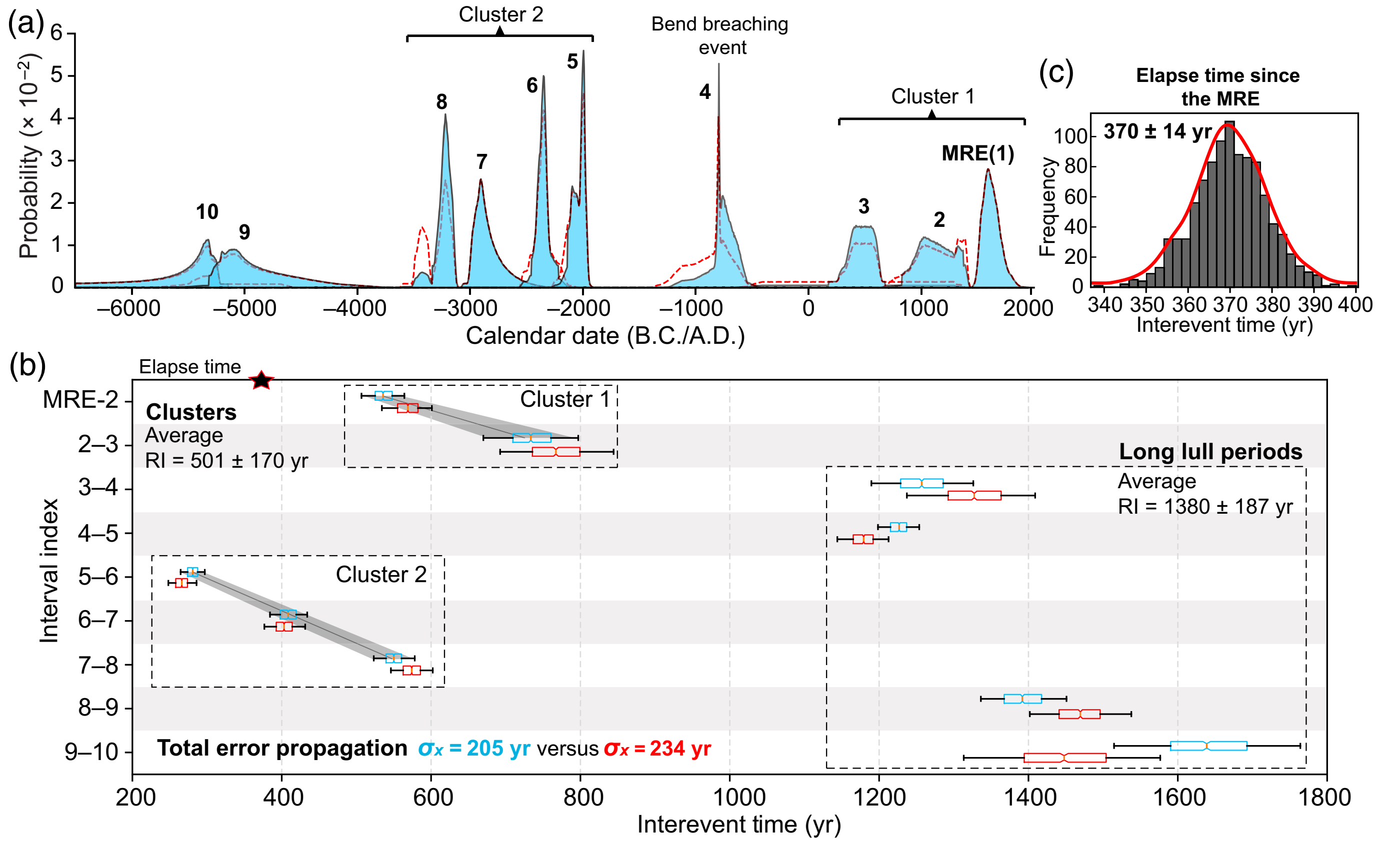

Figure 7. (a) Paleoearthquake time series of the central–eastern ATF. The blue-shaded curves correspond to PDFs obtained from the weighted-mean method. The open, red-dashed line curve represents event age PDFs from Pinzon *et al.* (2024), which are obtained using the conventional mean-PDF method of Biasi and Weldon (2009). (b) The box-and-whisker plot corresponds to the 95.5% confidence range of mean recurrence intervals between successive events in the earthquake chronology. The blue boxplots correspond to mean recurrence intervals between PDFs obtained using the weighted-mean method (solid light-blue curves). The red boxplots correspond to mean recurrence intervals from ages constrained by the mean method (open red-dashed curves). The light-gray line and stripe correspond to a least-square approximation and 2σ range confidence along recurrences in clusters 2 and 1. The black star represents the mean elapsed time. Average recurrence intervals (RI) are computed from weighted-mean PDFs. (c) Histogram representing the distribution of the current elapsed time since the most recent earthquake (MRE) occurred along the Xorxoli fault section (event 1). The color version of this figure is available only in the electronic edition.

From this analysis, we observed that the total uncertainty associated with the mean interevent times decrease from $\sigma_x = 234$ yr, when based on the mean-date PDFs, to $\sigma_x = 205$ yr using weighted-mean PDFs (red and blue values in Fig. 7b). The longest mean interval of 1635 yr, between events 10 and 9, is accompanied by large uncertainty, reflecting the broad 2σ ranges of those two events. It is important to note that events 9 and 10 were documented only in trenches on the northern strand of the ATF along the Aksai section, since trenches on the southern strand lack exposure of contemporaneous geological units; we cannot rule out the possibility of some paleoevents occurring between events 10 and 9 along the southern strand of the ATF. Therefore, it is possible that this interval does not represent a true seismic quiescence period but rather an unrecognized cluster phase in the early Holocene. If this interval is excluded, the average long-lull intervals is reduced to approximately 1294 yr.

Events 9 and 10 (Figs. 6i,j and 7a) provide another example. Their broad uncertainties increase the overall variance, and their substantial overlap further biases the average interevent time toward lower values (Fig. 7b). As a result, the mean-date estimate for this pair is ~250 yr shorter than the weighted-mean estimate. Therefore, by objectively combining paleoseismic data into better-constrained event ages, the weighted-mean method reduces age uncertainty and limits the influence of poorly constrained PDFs on recurrence-interval estimates. Finally, we used our MC to estimate the elapsed time between the most recent event (MRE) and the present year (2025), yielding an average of 370 ± 14 yr (Fig. 7c), almost as large as 40% of the mean recurrence intervals within cluster periods.

DISCUSSION

MUSIC provides a set of new tools to integrate paleoseismic data from multiple sites into a robust and well-constrained chronology that comprehensively describes the recurrence behavior of a fault system. A direct advantage of applying MUSIC is the ability to determine whether a fault system is prone to segmented earthquakes, multisection ruptures, or hybrid rupture behaviors. Such information is crucial for seismic hazard assessments, as it

constrains both the maximum expected earthquake size and the frequency at which major earthquakes may occur (Rockwell, 2010; Pinzón, 2025). A combined paleoearthquake time series serves as a primary input for developing more reliable time-dependent earthquake forecasting models, such as long-term fault memory approaches (Neely *et al.*, 2022). Furthermore, MUSIC provides better-constrained estimates of mean interevent times and elapsed times required to parameterize renewal processes, including Lognormal, Brownian Passage Time, and Weibull models (Hagiwara, 1974; Matthews *et al.*, 2002), as well as average recurrence intervals that are essential for developing
10 time-independent (Poisson-based) probabilistic seismic hazard models. During the last decade, paleoseismic observations and datasets have substantially increased (U.S. Geological Survey, 2020; Hürtgen *et al.*, 2021; Litchfield *et al.*, 2023), and the application of MUSIC will be fundamental for the proper integration of these data and the reliable reconstruction of fault rupture histories. This, in turn, provides an important opportunity to better constrain and evaluate current physics-based and kinematic–probabilistic earthquake sequence simulators (Zielke and Mai, 2023; Meade, 2024; Pinzón, 2025).

It is worthy to note that, in this work, we assume the rupture scenario proposed by Pinzon *et al.* (2024) as an input to introduce and test MUSIC. This rupture scenario was constrained using overlap-probability metrics and chronostratigraphic observations from individual trenches. Additional independent information was also incorporated, including historical records, chronologically constrained geomorphic offsets, and cumulative on-fault deformation markers. The rupture scenario most consistent with all available evidence was therefore considered the most likely fault rupture history along the ATF (Pinzon *et al.*, 2024). However, earthquake correlation remains an inherently cautious process, and it may not always be possible to exclude other plausible rupture correlations and objectively favor a single scenario over a set of alternative possibilities. This challenge is particularly relevant in regions lacking historical records, in areas containing multiple interacting active-fault systems (Cinti *et al.*, 2021; Williams *et al.*, 2024), or where dense vegetation and unfavorable climatic conditions obscure geomorphic offset markers (Reitman *et al.*, 2023). Given these limitations, we explicitly mention that MUSIC does not automatically generate or favor a preferred rupture scenario among all possible alternatives. The main reason is that there is no statistical metric that can prove a single "best" rupture scenario based solely on PDF analysis. Herein, we rather introduce the BC to reject potential event correlations with low likelihoods BC < 0.05. It further allows for identifying a set of plausible event correlations between sites (BC > 0.05), while quantifying their relative probabilistic support. Nevertheless, we acknowledge that this threshold might be sensitive to reject the null hypothesis that event correlations with BC > 0.05 are distinct events, which is also not necessarily always the case (as observed in Fig. 3b). Consequently, the complement of the Bhattacharyya coefficient (1−BC) may serve as a useful metric for evaluating the relative support for noncorrelation scenarios. Finally, the application of this metric should be guided by trench-based observations and consistency with empirical rupture length–slip relationships and fault-slip rates (Fig. 2a). Trench-based observations may include stratigraphic evidence (e.g., discontinuities and erosional surfaces), deformation indicators (e.g., the quality rank of primary and secondary deformation), and calibrated event ages to identify potential hiatuses. These lines of evidence are usually available in most paleoseismic trench investigations and provide a defensible basis for discriminating between more- or less-likely event correlations in the absence of independent constraints from historical records or previous studies.

Strain release accelerations during clustering periods along the ATF

The MUSIC framework provides new insights into the temporal behavior of large earthquakes along the ATF. The resulting unified chronology reveals systematic variations in recurrence intervals through time. Interestingly, during the two clustering phases, we observed that the mean interevent times exhibit a regular decrease over time (Fig. 7b), indicating a sustained increase in the frequency of large earthquakes. Least-squares approximations over recurrence intervals in cluster 2 suggest that successive earthquakes are characterized by progressively shorter recurrence intervals, decreasing by approximately 130–145 yr between events. A similar pattern appears in cluster 1, and the shortening rate observed in cluster 2 is consistent with that in cluster 1. If this pattern holds and given both the elapsed time since the MRE and the previous interevent time between events 2 and 1 (535 ± 37 yr; see Fig. 7b,c), it may suggest an elevated likelihood of a large earthquake occurring within the next few decades.

Additional statistical analysis of the revised ATF chronology yields an average memory coefficient (M) of 0.1 and an 11
average burstiness (B) (i.e., a normalized coefficient of variation; Goh and Barabási, 2008) of −0.22. These values suggest periods of substantial changes in earthquake recurrence, potentially associated with temporal variations of the slip rate along the fault system (Griffin *et al.*, 2020), which is consistent with the strain-release accelerations observed during the long-term clustering phases identified in our paleoearthquake time series. It is important to note, however, that memory and burstiness metrics exhibit variability arising from the chronological uncertainties of individual event ages (see Fig. S3). Therefore, we do not intend to suggest a prediction of occurrence, but rather to discuss the statistical significance of the observed recurrence behavior and highlight that, based on these findings, higher probabilities of a near-term event should be considered. On the other hand, it is also plausible to consider the possibility that the ATF is not currently within a clustered phase, but rather in the early stages of a millennial-scale quiescent period.

The accelerated strain-release phases observed in the ATF system could reflect complex fault interactions along the ATF. Mechanically, one possible explanation is that long-term stress transfer following a large earthquake can enhance differential stress and effectively increase strain rates along the adjacent fault sections. This additional loading may bring neighboring sections closer to failure, encouraging successive ruptures in relatively rapid succession. Along the central–eastern ATF, this could trigger a feedback loop in which ruptures on the NATF promote failure on the SATF, and vice versa, until the total accumulated regional strain budget is released (Stein, 1999; Dolan *et al.*, 2016; Mildon *et al.*, 2022). Another mechanism to consider is fault weakening during cluster periods. Oskin *et al.* (2008) proposed that the first earthquake in a cluster may drive fluid migration along the fault sections, thereby reducing its strength and promoting faster elastic strain accumulation in the crust. Once the stress level reaches the new, lowered fault strength, another rupture is triggered. Magnetotelluric research in the southeastern Tibetan plateau indeed suggests that crustal fluid migration may represent a key regional-scale seismogenic mechanism (Zhou *et al.*, 2025). Numerical simulations by Li *et al.* (2009) showed that as the fault zone continuously weakens during fluid accumulation, subsequent large events occur with a higher frequency. Then, once the weakening ceases and the system regains higher and constant fault strength, rupture recurrence shifts to much longer timescales, on the order of millennia, until sufficient strain is accumulated for the fault zone to start rupturing again.

Phases of accelerated strain release appear consistent with paleoslip-rate observations reported by Gold *et al.* (2017) along the central sections of the ATF. They documented a pulse of slip acceleration between 6.4 and 6.0 ka B.P. along the 85-km-long Cherchen He and 120-km-long Qin Shui fault sections, located roughly 70 km west of the Xorxoli section. This episode of enhanced slip, inferred from well-dated offset landforms, notably preceded the sequence of large earthquakes in cluster 2 (Fig. 7b). Hence, if the pulse of fault slip in the central ATF was the result of synchronized activation of adjacent fault sections as observed in the central–eastern ATF, it is therefore plausible that a broader, mid- to late-Holocene episode of earthquake clustering and long-term eastward migration of the seismicity could have occurred along the ATF system. Yet, this hypothesis remains to be further evaluated through additional paleoseismic investigations, both to determine whether the clustering behavior extends throughout the entire Holocene along the central–eastern ATF and to expand our understanding of past rupture behavior along the central ATF.

CONCLUSIONS

- We introduced MUSIC as a framework that aims to integrate paleoseismic data from multiple trench sites. MUSIC consists of two main stages such as (1) Correlation: we implemented the BC to quantitatively assess the degree of overlap between contemporaneous earthquake PDFs; and (2) Combination: we developed the weighted-mean method to objectively combine correlated PDFs into a unified paleoearthquake time series. This approach offers an opportunity to refine seismic hazard assessments and ultimately advance our understanding of rupture behavior along major continental fault systems worldwide. MUSIC also provides tools for paleoearthquake data analysis: (1) an MC approach to estimate the distribution of mean recurrence intervals from paleoseismic chronologies; and (2) the estimation of the coefficient of variation, burstiness (B), and memory coef- 12
ficient (M) while accounting for event-age uncertainties.
- The BC provides a normalized and symmetric measure of similarity ($0 \leq BC \leq 1$) based on the shape and temporal overlap between probability distributions. This method provides a useful probabilistic framework for: (1) rejecting correlations with very low likelihood ($BC < 0.05$); (2) identifying the set of plausible event correlations between sites ($BC > 0.05$) and quantifying their relative probabilistic support; and (3) evaluating support for noncorrelation through its complement (1–BC).
- The weighted-mean PDFs for the ten large earthquakes documented along the central–eastern ATF yield up to a 20% reduction in 2σ age uncertainties relative to the event dates derived from the mean method. Furthermore, the recurrence intervals derived from weighted-mean PDFs yield a 14% reduction in the propagation of the uncertainties compared with the recurrence estimates based on the mean-date PDFs. Unlike the product method, the weighted-mean approach yields a more representative age constraint by maximizing the probabilities on areas of PDF overlap while preserving the epistemic uncertainty of the full ensemble of observations.
- The analysis of the combined paleoearthquake chronology along the ATF shows a regular shortening of mean interevent times within cluster periods, where each interval is 130–145 yr shorter than the preceding one, until the system reaches a state of full relaxation and transitions into a long interseismic period. This systematic reduction in the mean interevent times may point to an acceleration of the earthquake cycle during cluster phases. Thus, if the central–eastern ATF is indeed currently in a seismic cluster phase and considering the most recent interevent time (370 ± 14 yr), our findings suggest an elevated probability of a new large earthquake occurring within the next few decades.

DATA AND RESOURCES

The multisite integrated chronologies (MUSIC) framework (Pinzon and Klinger, 2026) used for calculations in this research is preserved at doi: 10.5281/zenodo.20698918, maintained and openly developed 13
at https://github.com/nicolaspinzonmat/MUSIC. The MUSIC repository provides all the necessary scripts and data to facilitate the application of the proposed method to other paleoseismic datasets. Discrete

probability density functions used in this article came from published sources listed in the references. The supplemental material attached to this article contains Table S1 with event ages from each trench site and Figures S1 and S2 with interevent time histograms.

DECLARATION OF COMPETING INTERESTS

The authors acknowledge that there are no conflicts of interest recorded.

ACKNOWLEDGMENTS

The authors thank Jasper Moernaut and Maria Ortuño for providing constructive reviews on the structure and methodology of this work. The authors thank Muriel Livernet for the valuable comments on the mathematical aspects of the MUSIC. The authors are very thankful to the two reviewers, Jack Williams and Glenn Biasi, as well as Associated Editor Nicola Litchfield, and Editor-in-Chief Martin Mai, for their very constructive and thorough reviews that greatly contributed to improving the quality and clarity of this work.

REFERENCES

Benjelloun, Y., J. de Sigoyer, H. Dessales, S. Garambois, and M. Sahin (2018). Construction history of the aqueduct of Nicaea (Iznik, NW Turkey) and its on-fault deformation viewed from archaeological and geophysical investigations, *J. Archaeol. Sci.* **21,** 389–400, doi: 10.1016/j.jasrep.2018.08.010.

Bhattacharyya, A. (1943). On a measure of divergence between two statistical populations defined by their probability distributions, *Bull. Calcutta Math. Soc.* **35,** 99–109.

Biasi, G. P., and R. J. Weldon (2009). San Andreas fault rupture scenarios from multiple paleoseismic records: Stringing pearls, *Bull. Seismol. Soc. Am.* **99,** no. 2A, 471–498, doi: 10.1785/0120080287.

Biasi, G. P., R. J. Weldon II, T. E. Fumal, and G. G. Seitz (2002). Paleoseismic event dating and the conditional probability of large earthquakes on the southern San Andreas fault, California, *Bull. Seismol. Soc. Am.* **92,** no. 7, 2761–2781.

Bronk Ramsey, C. (1995). Radiocarbon calibration and analysis of stratigraphy: The OxCal program, *Radiocarbon* **37,** 425–30.

Bronk Ramsey, C. B. (2001). "Wiggle matching" radiocarbon dates, *Radiocarbon* **43,** 381–389.

Bronk-Ramsey, C. (2008). Deposition models for chronological records [Software], *Quat. Sci. Rev.* **27,** nos. 1/2, 42–60, doi: 10.1016/j.quascirev.2007.01.019.

Chinese State Bureau of Seismology (1992). *The Altyn Tagh Active Fault System*, Seismology Publishing House, Beijing, China, 319 pp. (in Chinese with English abstract).

Cinti, F. R., D. Pantosti, A. M. Lombardi, and R. Civico (2021). Modeling of earthquake chronology from paleoseismic data: Insights for regional earthquake recurrence and earthquake storms in the Central Apennines, *Tectonophysics* **816,** 229016, doi: 10.1016/j.tecto.2021.229016.

Dolan, J. F., L. J. McAuliffe, E. J. Rhodes, S. F. McGill, and R. Zinke (2016). Extreme multi-millennial slip rate variations on the Garlock fault, California: Strain super-cycles, potentially time-variable fault strength, and implications for system-level earthquake occurrence, *Earth Planet. Sci. Lett.* **446,** 123–136.

DuRoss, C. B., S. F. Personius, A. J. Crone, S. S. Olig, and W. R. Lund (2011). Integration of paleoseismic data from multiple sites to develop an objective earthquake chronology: Application to the Weber segment of the Wasatch fault zone, Utah, *Bull. Seismol. Soc. Am.* **101,** 2765–2781, doi: 10.1785/0120110102.

Elliott, A. J., M. E. Oskin, J. Liu-Zeng, and Y. Shao (2015). Rupture termination at restraining bends: The last great earthquake on the Altyn Tagh fault, *Geophys. Res. Lett.* **42,** no. 7, 2164–2170, doi: 10.1002/2015GL063107.

Gerstenberger, M. C., W. Marzocchi, T. Allen, M. Pagani, J. Adams, L. Danciu, E. H. Field, H. Fujiwara, N. Luco, K. F. Ma, *et al.* (2020). Probabilistic seismic hazard analysis at regional and national scales: State of the art and future challenges, *Rev. Geophys.* **58,** no. 2, e2019RG000653, doi: 10.1029/2019rg000653.

Goh, K. I., and A.-L. Barabási (2008). Burstiness and memory in complex systems, *EPL (Europhysics Letters)* **81,** no. 4, 48002.

Gold, R. D., E. Cowgill, J. R. Arrowsmith, and A. M. Friedrich (2017). Pulsed strain release on the Altyn Tagh fault, northwest China, *Earth Planet. Sci. Lett.* **459,** doi: 10.1016/j.epsl.2016.11.024.

Gómez-Novell, O., B. Pace, F. Visini, J. Faure Walker, and O. Scotti (2023). Deciphering past earthquakes from the probabilistic modeling of paleoseismic records—The paleoseismic earthquake chronologies code (PEACH, version 1), *Geosci. Model Dev.* **16,** 7339–7355, doi: 10.5194/gmd-16-7339-2023.

Griffin, J. D., M. W. Stirling, and T. Wang (2020). Periodicity and clustering in the long-term earthquake record, *Geophys. Res. Lett.* **47,** no. 22, e2020GL089272, doi: 10.1029/2020GL089272.

Gu, G. (1983). *Chinese Earthquake Catalog (1831 B.C.–1969 A.D.)*, Science Press, Beijing, 894 pp.

Guillerme, T., and N. Cooper (2016). Effects of missing data on topological inference using a total evidence approach, *Mol. Phylogenet. Evol.* **94,** 146–158.

Hagiwara, Y. (1974). Probability of earthquake recurrence as obtained from a Weibull distribution analysis of crustal strain, *Tectonophysics* **23,** 313–318, doi: 10.1016/0040-1951(74)90030-4.

Hürtgen, J., K. Reicherter, T. Spies, C. Geisler, and J. Schlittenhardt (2021). The paleoseismic database of Germany and adjacent regions PalSeisDB. V. 1.0, *GFZ Data Services*, doi: 10.5880/fidgeo.2020.040.

Klinger, Y., M. Le Beon, and M. Al-Qaryouti (2015). 5000 yr of paleoseismicity along the southern Dead Sea fault, *Geophys. J. Int.* **202,** no. 1, 313–327, doi: 10.1093/gji/ggv134.

Kremer, K., S. B. Wirth, A. Reusch, D. Fäh, B. Bellwald, F. S. Anselmetti, S. Girardclos, and M. Strasser (2017). Lake-sediment based paleoseismology: Limitations and perspectives from the Swiss Alps, *Quat. Sci. Rev.* **168,** 1–18.

Li, H., J. Pan, Z. Sun, D. Liu, J. Zhang, C. Li, K. Liu, C. Marie-Luce, K. Yun, and Z. Gong (2015). Seismogenic structure and surface rupture characteristics of the 2014 Ms 7.3 Yutian earthquake, *Acta Geol. Sinica* **89,** 180–194.

Li, Q., M. Liu, and S. Stein (2009). Spatiotemporal complexity of continental intraplate seismicity: Insights from geodynamic modeling and implications for seismic hazard estimation, *Bull. Seismol. Soc. Am.* **99,** no. 1, 52–60.

Lienkaemper, J. J., and C. Bronk-Ramsey (2009). OxCal: Versatil tool for developing paleoearthquake chronologies—A primer, *Seismol. Res. Lett.* **80,** no. 3, 431–434, doi: 10.1785/gssrl.80.3.431.

Litchfield, N. J., J. Humphrey, R. Morgenstern, R. M. Langridge, G. L. Coffey, and R. J. Van Dissen (2023). The New Zealand paleoseismic site database, version 1.0, *Seismol. Res. Lett.* **95,** 64–77, doi: 10.1785/0220230150.

Luo, H., X. Xu, Z. Gao, X. Liu, H. Yu, and X. Wu (2019). Spatial and temporal distribution of earthquake ruptures in the eastern segment of the Altyn Tagh fault, China, *J. Asian Earth Sci.* **173,** 263–274, doi: 10.1016/j.jseaes.2019.01.005.

Matthews, M. V., W. L. Ellsworth, and P. A. Reasenberg (2002). A Brownian model for recurrent earthquakes, *Bull. Seismol. Soc. Am.* **92,** 2233–2250, doi: 10.1785/0120010267.

Meade, B. J. (2024). A kinematic method for generating earthquake sequences, *Comput. Geosci.* **184,** 105517, doi: 10.1016/j.cageo.2023.105517.

Mildon, Z. K., G. P. Roberts, J. P. Faure Walker, J. Beck, I. Papanikolaou, A. M. Michetti, and E. Vittori (2022). Surface faulting earthquake clustering controlled by fault and shear-zone interactions, *Nat. Commun.* **13,** no. 1, 7126.

Neely, J. S., L. Salditch, B. D. Spencer, and S. Stein (2022). A more realistic earthquake probability model using long-term fault memory, *Bull. Seismol. Soc. Am.*, doi: 10.1785/0120220083.

Oskin, M., L. Perg, E. Shelef, M. Strane, E. Gurney, B. Singer, and X. Zhang (2008). Elevated shear zone loading rate during an earthquake cluster in eastern California, *Geology* **36,** no. 6, 507–510.

Pinzón, N. (2025). Spatial temporal organization of large earthquakes along continental fault systems, *Ph.D. Thesis*, Earth Sciences, Université Paris Cité, 270 pp. (see chapter 7, 264 pp.), doi: 10.70675/263e9cdczdbe9z4cd1zbdddzcd0f1d4af799.

Pinzon, N., and Y. Klinger (2026). MUSIC (multisite integrated chronologies), *Zenodo*, doi: 10.5281/zenodo.20698919.

14 Pinzón, N., and C. A. Vargas (2021). Global variation of seismic energy release with oceanic lithosphere age, *Sci. Rep.* **11,** 601, doi: 10.1038/s41598-020-80475-y.

Pinzon, N., Y. Klinger, X. Xu, P. Tapponnier, J. Liu-Zeng, J. Van Der Woerd, K. Li, and M. Gao (2024). Spatiotemporal clustering of large earthquakes along the central-eastern sections of the Altyn Tagh fault, China, *J. Geophys. Res. Solid Earth* **129,** e2024JB028912, doi: 10.1029/2024JB028912.

Reitman, N. G., Y. Klinger, R. W. Briggs, and R. D. Gold (2023). Climatic influence on the expression of strike-slip faulting, *Geology* **51,** no. 1, 18–22, doi: 10.1130/G50393.1.

Rockwell, T. K. (2010). A long record of earthquakes with timing displacements for the dead-sea transform fault: A test of earthquake recurrence models, *NSF Award Number 1019871. Directorate for Geosciences* 10, no. 1019871, 19,871 pp.

Scharer, K. M., R. J. Weldon, T. E. Fumal, and G. P. Biasi (2007). Paleoearthquakes on the southern San Andreas fault, Wrightwood, California, 3000 to 1500 B.C. A new method for evaluating paleoseismic evidence and earthquake horizons, *Bull. Seismol. Soc. Am.* **97,** no. 4, 1054–1093, doi: 10.1785/0120060137.

Shao, Y., J. Liu-Zeng, M. E. Oskin, A. J. Elliott, P. Wang, J. Zhang, Z. Yuan, and Z. Li (2018). Paleoseismic investigation of the Aksay restraining double bend, Altyn Tagh fault, and its implication for Barrier-breaching ruptures, *J. Geophys. Res. Solid Earth* **123,** no. 5, 4307–4330, doi: 10.1029/2017JB015397.

Stein, R. S. (1999). The role of stress transfer in earthquake occurrence, *Nature* **402,** 605–609.

Stirzaker, D. (2003). *Elementary Probability*, Cambridge University 15
Press, 24–50.

U.S. Geological Survey (2020). Quaternary fault and fold database for the nation, doi: 10.5066/P9BCVRCK.

Wang, T., J. D. Griffin, M. Brenna, D. Fletcher, J. Zeng, M. Stirling, P. W. Dillingham, and J. Kang (2024). Earthquake forecasting from paleoseismic records, *Nat. Commun.* **15,** no. 1, 1–12.

Washburn, Z., J. R. Arrowsmith, G. Dupont-Nivet, W. X. Feng, Z. Y. 16
Qiao, and C. Zhengle (2003). Paleoseismology of the Xorxol segment of the central Altyn Tagh fault, Xinjiang, China, *Ann. Geophys.* **46,** 1015–1034.

Washburn, Z., J. R. Arrowsmith, S. L. Forman, E. Cowgill, W. 17
Xiaofeng, Z. Yueqiao, and C. Zhengle (2001). Late Holocene earthquake history of the central Altyn Tagh fault, China, *Geology* **29,** no. 11, 1051–1054.

Wechsler, N., T. K. Rockwell, Y. Klinger, P. Stepancikova, M. Kanari, S. Marco, and A. Agnon (2014). A paleoseismic record of earthquakes for the Dead Sea Transform fault between the first and seventh centuries CE: Nonperiodic behavior of a plate boundary fault, *Bull. Seismol. Soc. Am.* **104,** 1329–1347.

Wells, D. L., and K. J. Coppersmith (1994). New empirical relationships among magnitude, rupture length, rupture width, rupture area, and surface displacement, *Bull. Seismol. Soc. Am.* **84,** 974–1002.

Williams, J., M. Stirling, R. Langridge, G. Niroula, A. Vause, J. Stewart, A. Nicol, and N. Wang (2024). Along-strike extent of earthquakes on multi-segment reverse faults; insights from the Nevis-Cardrona fault, Aotearoa New Zealand, *Seismica* **3,** no. 2, doi: 10.26443/seismica.v3i2.1310.

Xu, X., X. Tan, G. Wu, J. Chen, J. Shen, W. Fang, and H. Song (2011). Surface rupture features of the 2008 Yutian M_S 7.3 earthquake and its tectonic nature, *Seismol. Geol.* **33,** 462–471.

Yuan, Z., J. Liu-Zeng, W. Wang, R. J. Weldon II, M. E. Oskin, Y. Shao, Z. Li, Z. Li, P. Wang, and J. Zhang (2018). A 6000-year-long paleoseismologic record of earthquakes along the Xorxoli section of the Altyn Tagh fault, China, *Earth Planet. Sci. Lett.* **497,** 193–203.

Zhou, Z., N. Yu, T. Wang, W. Kong, H. Chen, and T. Li (2025). Episodic earthquakes controlled by the migration of crustal fluids and fault valve behavior, *Geophys. Res. Lett.* **52,** e2024GL114093, doi: 10.1029/2024GL114093.

Zielke, O., and P. M. Mai (2023). MCQsim: A multicycle earthquake simulator, *Bull. Seismol. Soc. Am.* **113,** no. 3, 889–908.

Manuscript received 26 March 2026